

Supporting Information

Localized mechanical stimulation of single cells with engineered spatio-temporal profile

M. Monticelli¹, D. S. Jokhun², D. Petti¹, G. V. Shivashankar^{2,3,4} and R. Bertacco^{1,5}

¹*Department of Physics, Politecnico di Milano, Milan, Italy*

²*Mechanobiology Institute, National University of Singapore, Singapore*

³*Department of Biological Sciences, National University of Singapore, Singapore*

⁴*Institute of Molecular Oncology, Italian Foundation for Cancer Research, Milan, Italy*

⁵*IFN-CNR, c/o Politecnico di Milano, Milan, Italy*

S1. Micromagnetic configurations of magnetic pillars and force calculation

The micromagnetic configuration of magnetic pillars (see Fig.S3) has been simulated with the software OOMMF (Object Oriented MicroMagnetic Framework), using standard parameters for *Fe* (see *Methods*) and considering null magnetocrystalline anisotropy. This latter assumption is supported by the magnetic characterization of the pillars performed by Vibrating sample magnetometry (see the next section and Fig.S4), showing that the deposited *Fe* is magnetically isotropic.

Micromagnetic configurations are calculated for a couple of adjacent pillars, when $\mu_0 H_e = 50$ mT is directed at 0, 45 and 90 degrees (Fig.S3a-c) with respect to the *x*-axis connecting the center of the two pillars. In all cases, **M** is aligned to the external field, resulting in a mono domain configuration of *Fe*-disks. Similar single-domain configurations are simulated for $\mu_0 H_e$ ranging between 10 and 100 mT. Hence, *Fe*-disks act as two magnetic dipoles, experiencing a magnetic force (**F_M**) which induces pillars bending (see main text).

Besides, the magnetic configuration in remanence, i.e. 0 field applied, has been simulated upon application and removal of a saturating **H_e** along the positive direction of *x*-axis (see Fig.S3d). In this case, we obtain a multi-domains configuration where **M** is no more uniformly aligned. The magnetic force (see *Methods*) exerted in this case is $F_M = 1.2$ nN (attractive), much lower than the maximum value for $\mu_0 H_e = 50$ mT, thus indicating that the hysteretic behavior of *Fe*-disks has a reduced effect on **F_M**.

At first approximation, the total force acting on a single pillar can be calculated just by considering the interaction between first neighbors pillars and neglecting the interaction along the diagonal of the square. To support this claim, we calculated the force between two pillars along the diagonal, magnetized by an external field $\mu_0 H_e = 50$ mT along the *x*-axis, as in Figure S3e. The magnetic force is attractive and directed along the diagonal, but the intensity is just 2.15 nN. This is negligible,

when compared to F_x and F_y (see Fig.2d) resulting from the same \mathbf{H}_e (directed at $\phi = 0$ deg), which are on the order of 50 and 15 nN, respectively.

In order to estimate the effective force applied on the cells, we consider the total force (\mathbf{F}_{TOT}) acting on the top Fe -disk of each pillar, when a cell is cultured on top (as in Fig.2a). \mathbf{F}_{TOT} takes into account three different contributions: the magnetic force (\mathbf{F}_M), the pillars elastic force (\mathbf{F}_{el}) which opposes \mathbf{F}_M , and \mathbf{F}_{cell} , which is the force exerted by the cell on the pillar. At equilibrium, $\mathbf{F}_{\text{TOT}} = \mathbf{F}_{el} + \mathbf{F}_M + \mathbf{F}_{cell} = 0$. At first approximation, this equation holds true also in our experiments, because \mathbf{H}_e rotates slowly and each configuration in Figure 2a can be considered as stationary. In the following, we evaluate the x -component of \mathbf{F}_{cell} when $\mu_0 H_e = 50$ mT is applied along the horizontal direction (x -axis, Fig.2a). First, \mathbf{F}_M is calculated via micromagnetic simulations (see Methods), thus giving $F_x = 47.8$ nN (attractive, see Fig.2d) which is the maximum magnetic force on pillars during pinching (see the main text). Besides, \mathbf{F}_{el} is evaluated from the experimental deflections extrapolated by the optical images (see Figure 2a in the main text) when the pillars are interacting with a cell plated on top, according to the elastic model¹ discussed in the main text. Considering the distances between adjacent pillars centers along the x -axis (x_i) for the pillars configurations reported in frames 1 (x_1) and 2 (x_2) in Figure 2a, we calculated $\Delta x = x_2 - x_1 \approx 230$ nm. Note that, this value is not exactly the maximum deflection along- x from the rest position because in frame 2 a weak attractive force is still experimented by pillars along the same direction (≈ 11 nN, when \mathbf{H}_e is applied at 45 degrees, see Fig.2d). In this set of experiment the value at $\mu_0 H_e = 0$ was inaccessible, due to the presence of permanent magnets mounted around the sample holder. Nevertheless, the force when \mathbf{H}_e is at 45 degrees is much smaller than that when the maximum \mathbf{H}_e is applied at 0 degrees, thus allowing to take our Δx value as a good approximation of the deflection with respect to the true equilibrium position at zero field. With this assumption, the elastic force is calculated according to $F_{el} = (k \cdot \Delta x) / 2$, where $k = (3/64)\pi E D^4 / H^3$ is the elastic constant extracted from the fit of Figure 1g (red dashed-line) in the main text. F_{el} is about 27 nN, and a rough estimation for the net maximum force acting on the cell can be calculated as $F_{x-cell} = F_x - F_{el} \approx 20$ nN.

S2. Magnetic characterization of the device

The magnetic properties of the active substrate have been measured by Vibrating Sample Magnetometry (VSM). To investigate possible magnetic anisotropy, hysteresis loops have been recorded for different orientations of the external field (\mathbf{H}_e), applied in the device plane, with steps of 10 degrees. Negligible differences in the magnetic response at different ϕ are found, in terms of loops shape, saturation magnetization and coercive field (H_c). The typical hysteresis loop is reported in Fig.S4a. From this hysteresis loop, $\mu_0 H_c = 5.3$ mT is extrapolated and similar values are found at

different angles, as shown in the polar diagram of H_c (see Fig.S4b). The maximum variation in the value of H_c is less than 3%, thus indicating a negligible magnetic anisotropy of iron deposited on PDMS. Both shape anisotropy and magnetocrystalline anisotropy are thus negligible, as assumed in our micromagnetic simulations.

Note that, due to the fabrication process, Fe is deposited not only on top of pillars but also on the PDMS basement. This contribution can affect the magnetic response of the whole device and plays a role in the resulting hysteretic behavior observed in Fig.S4a. However, the experiments performed to evaluate the deflection of pillars (see Fig.1e,f) have not shown a relevant hysteretic behavior and this is confirmed by the micromagnetic simulation of Fe -disks in remanence (null field), demonstrating that a negligible magnetic force between a couple of adjacent pillars results in this case (see section S1 and Fig.3d)."

Moreover, the Fe layer at the bottom of pillars has a negligible impact on the force between top Fe -disks, due to the relatively large distance (10 μm) between the top and the bottom, as compared to that between adjacent disks (2 μm).

S3. Force transduction to the nucleus regulated by active biological processes

As discussed in the main text, the nuclear shape evolution displays slow dynamics, over a time scale much longer than the period (T_p) of pinching. This suggests that the effect of mechanical stimulation on the membrane is transferred to the nucleus by active cellular processes, mediated by the cytoskeleton, and not via a direct elastic coupling between pillars and nucleus. To confirm this assumption, in Figure S8 we compare the normalized nuclear area fluctuations (see the main text) during pinching (acquired at 0.5 fps to precisely capture their oscillations in time) and the mechanical stress arising from pinching (at $f_p= 0.1$ Hz). The x -component of the strain field has been rescaled between ± 1 , in order to properly compare the amplitude of the force field with the normalized area fluctuations. Data have been acquired for 20 min on 10 different cells, to achieve a reasonable statistics. To estimate the correlation between the two curves, the Pearson correlation coefficient² c has been calculated for each of the 10 cells. The average value is $c= 0.05\pm 0.03$, indicating that the two curves are uncorrelated. This demonstrates that a weak elastic coupling between pillars and nucleus exists, so that the nucleus area fluctuations are not directly affected by the strain field oscillating at the pinching frequency.

S4. H2B-EGFP images correlation

To understand how the mechanical stimuli induced by magnetic pillars influence protein dynamics inside the cell nucleus, we performed FRAP (see main text) and images correlation analyses on

H2B-EGFP positive nuclei. The latter consists in the calculation of the pixel-by-pixel correlation of H2B core histone images with respect to an initial reference frame (*see Methods*). The correlation coefficient is calculated for each nucleus as a function of time. With a similar procedure to the one used for RFP-Lifect images (see the main text), we calculated the correlation coefficient with respect to a reference frame at $t=0$ min, acquiring images during the following 20 minutes with a rate of 3 frames per minute. Figure S9a shows the correlation coefficients for 10 different H2B-EGFP nuclei without (black curves) and with (red curves) mechanical pinching. The reference frame during pinching corresponds to the time-point at which the rotation of \mathbf{H}_e is switched on. Figure S9b shows the average correlation coefficient for the 10 nuclei. An enhancement in H2B images de-correlation was observed during pinching. In order to quantify this aspect, we performed a linear fit of the correlation coefficient (as function of time) for each nucleus. The average absolute value of fitting lines slope, $|dc/dt|$ (see the inset in Fig.S9b) is around 2.6 times higher during pinching, indicating a relevant increase of H2B images de-correlation. Furthermore, the de-correlation curve during pinching is still decreasing in a linear way after 20 min. This suggests a persisting enhanced dynamic behavior of nucleus during stimulation. Finally, note that the higher variability from the mean of $|dc/dt|$ during pinching than before pinching (see inset in Fig.S9b) is in agreement with the enhancement of nucleus dynamics.

Image correlation analysis provides useful information on nuclear behavior during stimulation. However, it cannot disentangle two different contributions to decorrelation: changes in nucleus morphology and variation of H2B intensity inside the nucleus. On the other hand, properly investigating the H2B dynamics inside the nucleus is crucial, as alterations in H2B turnover on chromatin affects genomic functions such as transcription. At this purpose, FRAP analysis of H2B-EGFP was performed, as discussed in the main text.

S5. Visco-elastic model of the cell nucleus

The biological responses of stimulated cells are consistent with the physical properties of nucleus and cytoskeleton, according to a simplified Kelvin-Voigt (see Fig.S11) model for the nucleus, considered as a viscoelastic body with a certain viscosity η and Young modulus E . The Kelvin-Voigt approach is preferred to more complex models (e.g. Jeffrey's model³), because it provides valuable information when slow and saturating dynamics, such as the alteration of nucleus shape observed in our work, occur. The nucleus experiences a variation of the stress exerted by the cytoskeleton when cells are mechanically stimulated. According to the Kelvin-Voigt model, the equation describing the visco-elastic behavior of a body is:

$$\sigma(t) = E\varepsilon(t) + \eta \frac{\partial \varepsilon}{\partial t} \quad (S1)$$

where σ is the mechanical stress applied on the nucleus and ε is the nuclear strain. Considering the simplified case of uniform and constant stress applied on the nucleus during pinching (σ_0), we evaluated the nucleus response as function of time, as follows:

$$\varepsilon(t) = \varepsilon_0 - \Delta\varepsilon(1 - e^{-t/\tau}) \quad (S2)$$

where $\tau = \eta/E$ is the response time-constant. According to the results illustrated in Figure 3b-d in the main text, nuclei move to a lower eccentricity status with a time-constant of ~ 100 s. Fibroblasts nuclear viscosity (η) is about 10 kPa⁴, from which we can extract the nuclear Young Modulus $E \approx 100$ Pa, in agreement with typical fibroblasts nucleus stiffness³. This simple model enforces the biological findings, providing a physical basis to the cell response.

S6. Statistical analysis

We performed statistical tests to demonstrate the significance of the biological results found in this paper.

For the analysis on nuclear eccentricity (see Fig.3), the statistical significance was shown with a *T*-test on the nuclear eccentricity difference (during and before pinching, $\delta = \varepsilon_{DP} - \varepsilon_{BP}$), which gives the probability that acquired data are representative of a population with $\delta \neq 0$. In this case, the test is given by the value $t = |\langle \delta \rangle - 0| \cdot \sqrt{n} / \sigma_\delta = 13.5$, where $\langle \delta \rangle$ is the mean of the eccentricity difference, σ_δ is the standard deviation of the difference (δ) and n is number of samples (10 in our case). For this test, a significance level larger than 99.999% was calculated, thus confirming that there is a statistically significant difference before and during pinching.

For the area fluctuation analysis in Figure 4, we performed a *F*-test on the variances of PNAF before and during pinching with $F = (\sigma_{DP})^2 / (\sigma_{BP})^2 = 4.9$. This test reports the probability that the two distributions (before and during pinching) have the same variance. For this *F*-test, we calculated a *p-value* < 0.001 , which clearly points out that pinching induces larger area fluctuations.

For statistical significance of MKL intensity in Figure 5, we performed *T*-test for the MKL intensity ratio ($r = I_{DP} / I_{BP}$) in the cytoplasm and nucleus, to show the probability that data are representative of a population with $r < 1$ for the nucleus and $r > 1$ for the cytoplasm, as emerges by MKL shuttling outside the nucleus during pinching. In this case, $t = (\langle r \rangle - 1) \cdot \sqrt{n} / \sigma_\delta$, where $\langle r \rangle$ is the mean of the signal intensity ratio, σ_δ is the standard deviation of r and $n = 10$ is the number of samples. $t_{\text{cytoplasm}} = 7.7$ and $t_{\text{nucleus}} = 13$ were calculated, corresponding to a significance level larger than

99,999% in both the two cases. Indeed, this analysis confirms that MKL translocation induced by pinching is statistically significant.

References

¹Ghibaudo, M. et al. Traction forces and rigidity sensing regulate cell functions. *Soft Matter* **4**, 1836-1843 (2008).

²Mukaka, M. Statistics corner: A guide to appropriate use of correlation coefficient in medical research. *Malawi Medical Journal*, **24**, 3, 69-71 (2012).

³Bausch, A., et al. Local measurements of viscoelastic parameters of adherent cell surfaces by magnetic bead microrheometry. *Biophys J.* **75**, 2038–2049 (1998).

⁴Guliyak, F., Tedrow, J. R. & Burgkart, R. Viscoelastic properties of the cell nucleus. *Biochemical and Biophysical Research Communications* **269**, 781–786 (2000).

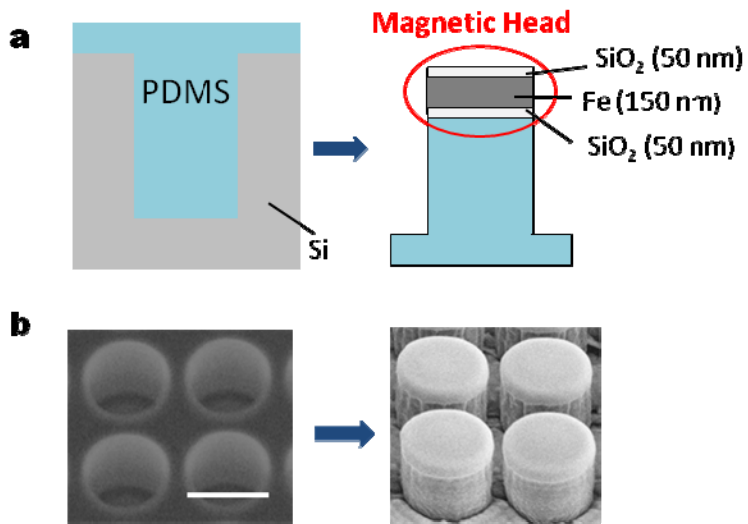


Figure S1: **a** Sketch of the magnetic pillars fabrication process: PDMS is cast on a *Si* mold and, after curing, it is peeled out; subsequently a trilayer of SiO_2 (50 nm) / Fe (150 nm) / SiO_2 (50 nm) is deposited by e-beam evaporation. **b** Scanning electron microscopy (SEM) images showing the mold and the coated pillars.

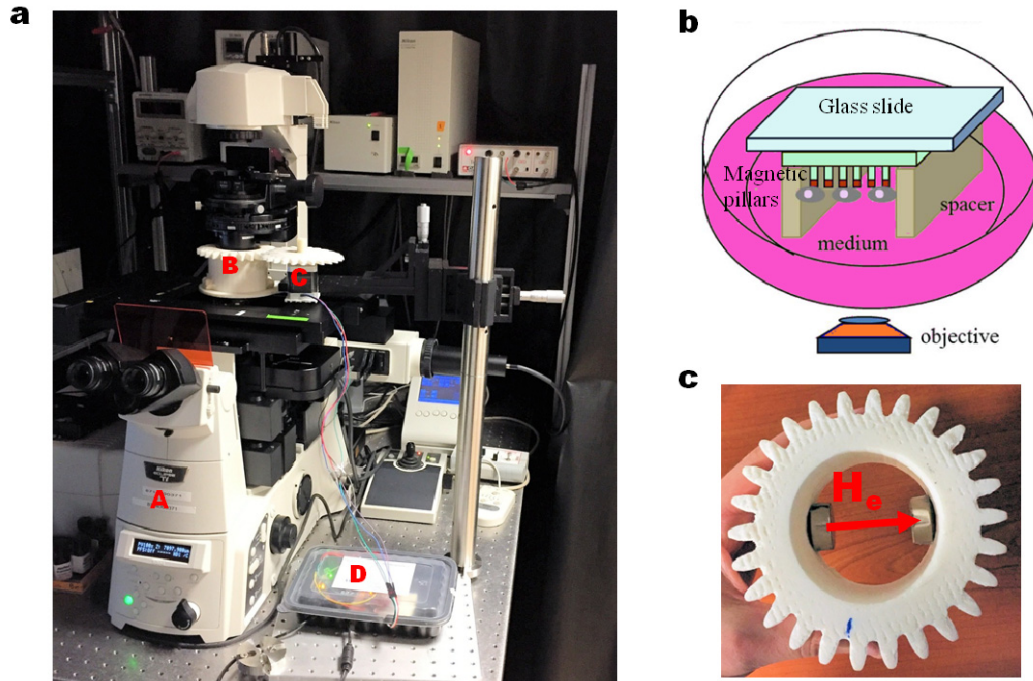


Figure S2: **a** Setup used for the biological experiments showing the fluorescence *Nikon AIR* Confocal microscope (**A**), the 3D-printed holder for permanent magnets (**B**), a stepper motor (**C**) allowing the field rotation, properly controlled by an *Arduino-UNO* microcontroller (**D**). **b** Sketch of the petri dish containing the device and the cultured cells; the chip is turned upside-down on two spacers for performing imaging with the inverted microscope. **c** Detail of the magnets holder which allows for the application of a uniform and rotating magnetic field (H_e).

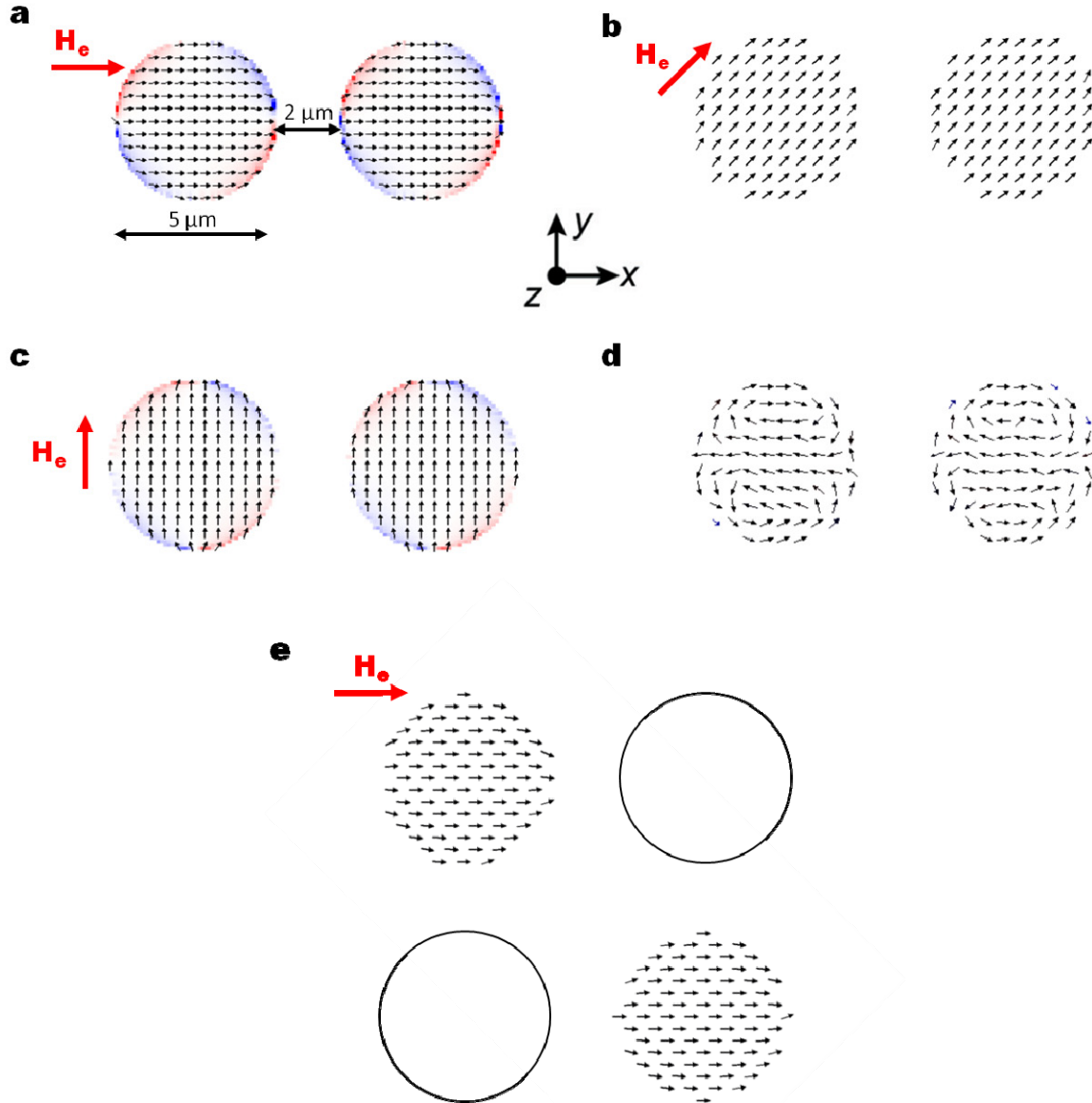


Figure S3: Micromagnetic configurations (simulated using OOMMF) of two adjacent *Fe*-disks on top of PDMS pillars, when an external magnetic field ($\mu_0 H_e = 50$ mT) oriented at 0, 45, 90 degrees (**a**, **b**, **c**) with respect to the *x*-axis is applied. In **d**, micromagnetic configuration in remanence, after the application of a saturating \mathbf{H}_e along the *x*-axis. **e** Magnetic configuration of *Fe*-disks on the diagonal of a 4-pillars group. The arrows represent the local magnetization direction, while the red-white-blue scale color in **a** (and **c**) refers to the *y*-component (and *x*-component) of the magnetization. **e** Micromagnetic configuration of two pillars along the diagonal of the square, with applied magnetic field $\mu_0 H_e = 50$ mT, directed along the *x*-axis.

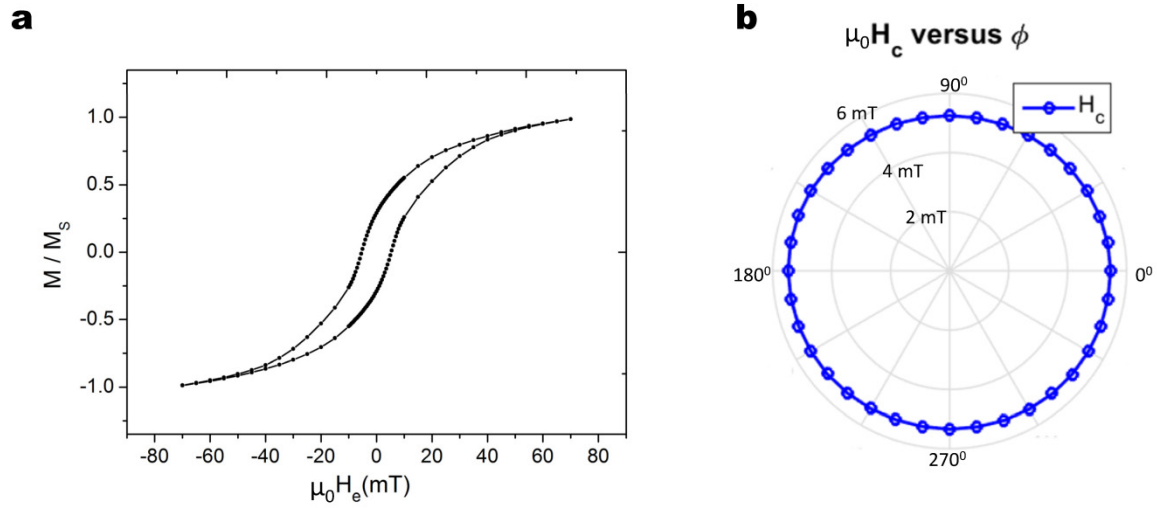


Figure S4: **a** Hysteresis loop of the active substrate. The magnetization M is normalized to the saturation magnetization M_s . **b** Polar diagram showing the coercive field (H_c) as function of the angle (ϕ) between the sample side and the external field H_e .

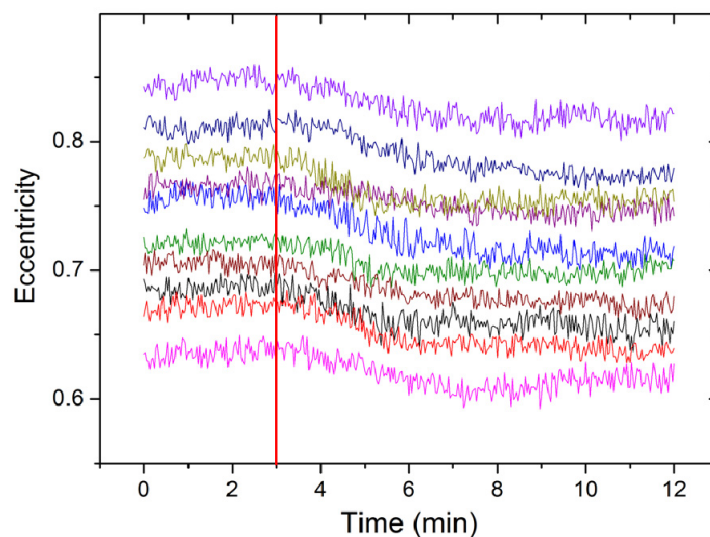


Figure S5: a Nucleus projected area eccentricity as function of time measured for $n=10$ cells (data acquired in three different experiments), before ($t=0-3$ min) and during ($t=3-12$ min) pinching. The red line shows the time at which the rotation of the external magnetic field (\mathbf{H}_e) is turned on. In response to the application of mechanical stimuli, the eccentricity decreases, thus resulting in less elongated nuclei.

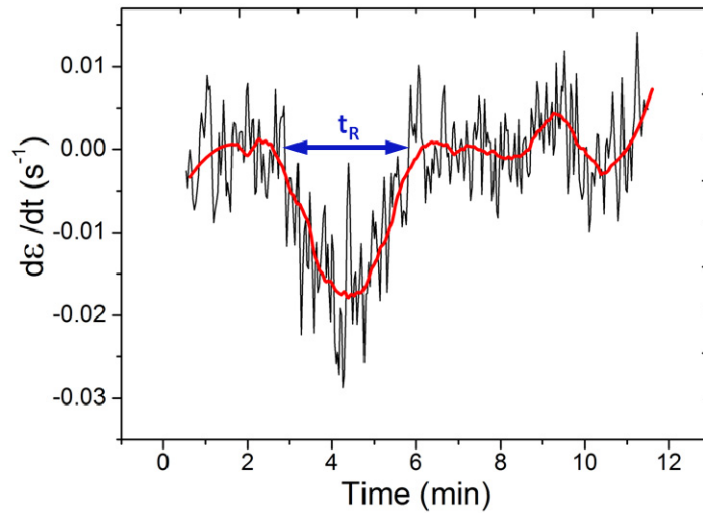


Figure S6: Derivative of nucleus projected area eccentricity ($d\epsilon/dt$), smoothed with Savitzky-Golay filter (5 points) to evaluate the "well" width, which corresponds to the transition time t_R (see Fig.3b,d) of the nucleus to a less elongated state. The transition time for each nucleus (see Fig.3d) is calculated with an error of ± 20 s, arising by the accuracy with which is possible to extract the well width from the data.

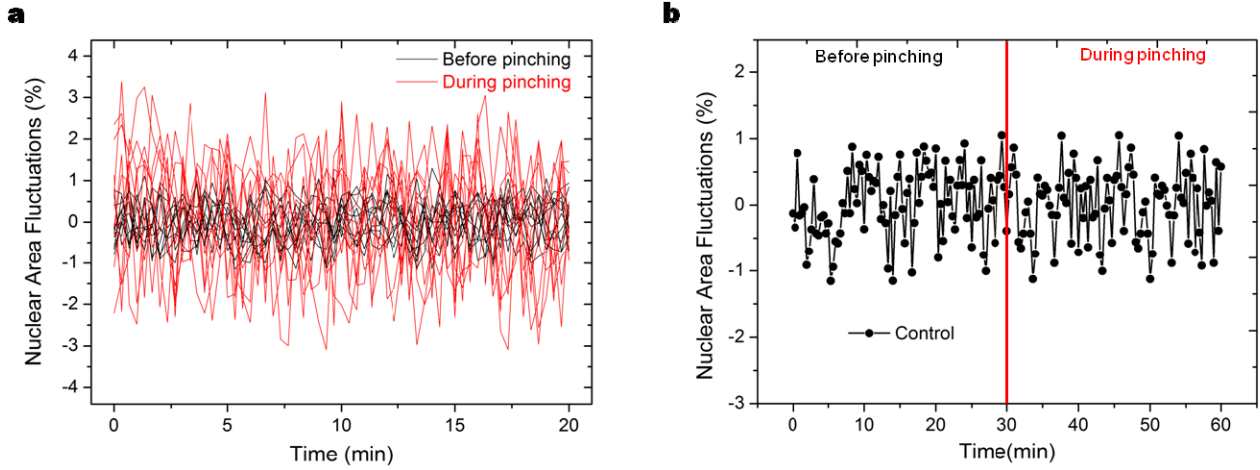


Figure S7: a Percentage nuclear area fluctuations (PNAFs) vs. time measured for $n=10$ cells (data acquired in four different experiments), before (black curves) and during pinching (red curves). **b** PNAFs vs time, measured on a cell cultured on non-magnetic (without Fe -coating) PDMS micropillars in a control experiment. The red line represents the time at which rotation of $\mu_0 H_e = 50$ mT is turned on.

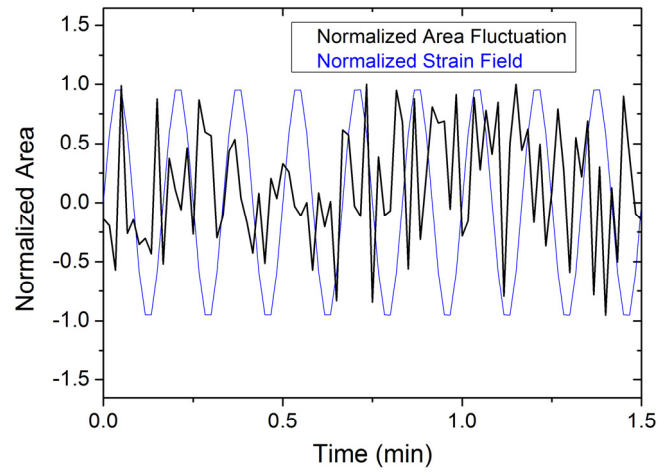


Figure S8: Normalized nuclear area fluctuations and x -component of the stress field as function of time. The strain field oscillates at the pinching frequency ($f_p = 0.1$ Hz).

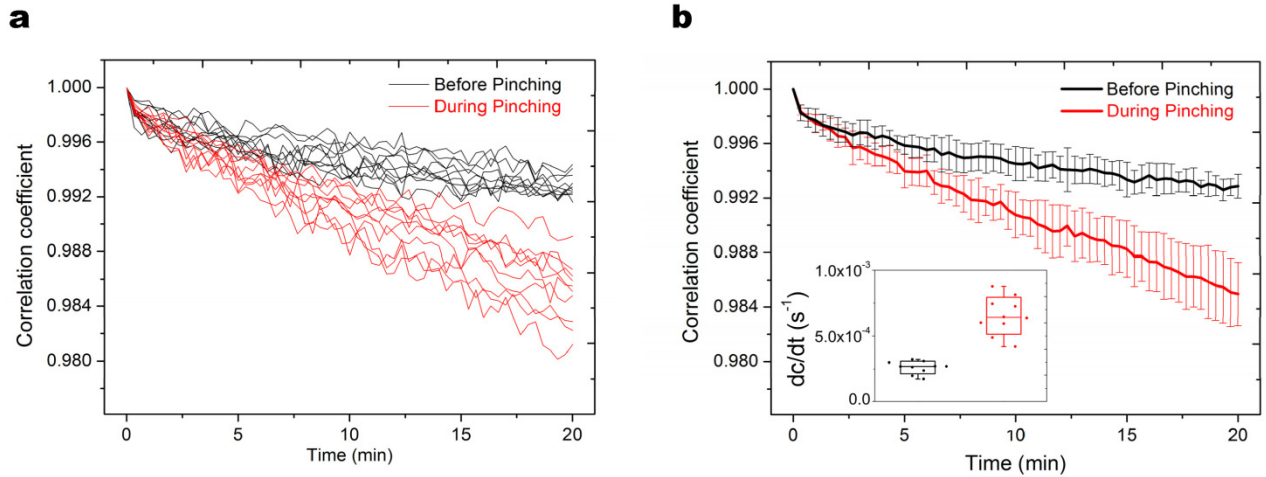


Figure S9: a Images correlation coefficient vs. time of H2B-EGFP green fluorescent nuclei with respect to a reference frame (at $t=0$ min), before (black) and during (red) pinching, calculated for $n=10$ distinct cells (data acquired in four different experiments). The correlation coefficient is calculated according to Equation 3, performing a pixel-by-pixel analysis. The reference frame ($t=0$ min) of the analysis “during pinching” is that taken when the rotation of the magnetic field is turned on. Error bars represent the standard deviations from the mean. **b** Correlation coefficient vs time averaged over $n=10$ cells reported in panel a. The inset shows box plots for the linear fitting of images correlation coefficient slopes (dc/dt), calculated for the $n=10$ cells, before (black) and during (red) pinching. The bottom and top of the box represent the first and third quartiles, whereas the line represents the median. The ends of the whiskers correspond to the lowest/highest data point of the distribution.

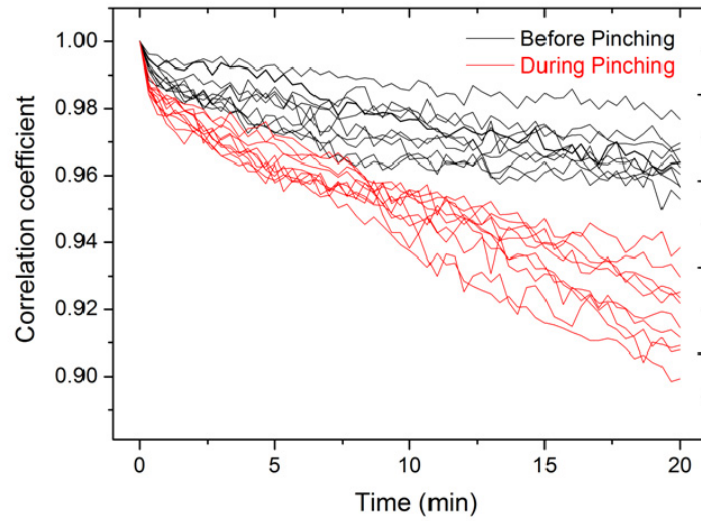
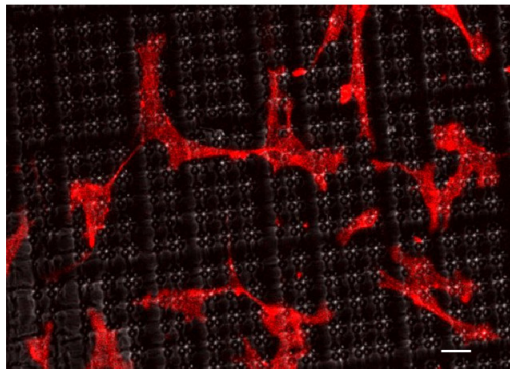


Figure S10: Images correlation vs time of RFP-Lifeact red fluorescent cells, before (black) and during (red) pinching, calculated for $n=10$ cells (data acquired in four different experiments). The correlation coefficient is calculated according to Equation 3, performing a pixel-by-pixel analysis. The reference frame (at $t=0$ min) for the analysis “during pinching” is that taken when the rotation of the magnetic field is turned on.

a

Day 1

**b**

Day 3 (3h after cell-split)

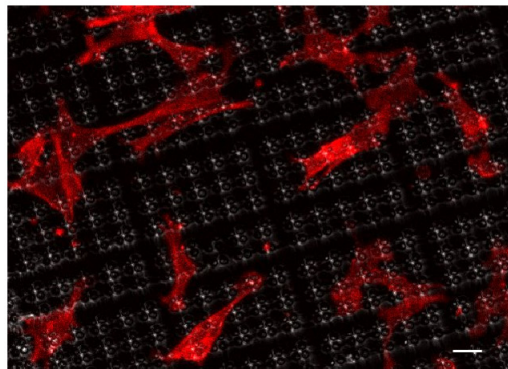


Figure S11: Confocal microscopy images showing NIH3T3 cells (stained with RFP-lifeact) cultured on magnetic pillars at day 1 (**a**) and at day 3 (**b**). Scale bar: 20 μm .